The impact threshold of the aerosol radiative forcing on the boundary layer structure in the pollution region

Dandan Zhao[†1,2], Jinyuan Xin[*†1,2,3], Chongshui Gong[4], Jiannong Quan[5], Yuesi Wang[1,2], Guiqian Tang[1], Yongxiang Ma[1], Lindong Dai[1], Xiaoyan Wu[1], Guangjing Liu[1], Yongjing Ma[1]

1. State Key Laboratory of Atmospheric Boundary Layer Physics and Atmospheric Chemistry (LAPC), Institute of Atmospheric Physics, Chinese Academy of Sciences, Beijing 100029, China

2. University of Chinese Academy of Sciences, Beijing 100049, China

3. Collaborative Innovation Center on Forecast and Evaluation of Meteorological Disasters, Nanjing University of Information Science and Technology, Nanjing, 210044, China

4. Institute of Arid Meteorology, China Meteorological Administration, Lanzhou 730020, China

5. Institute of Urban Meteorology, Chinese Meteorological Administration, Beijing, China

(†) These authors contributed equally to this study.

(*) **Correspondence to:** Jinyuan Xin (xjy@mail.iap.ac.cn).

1   **Abstract:** Recently, there has been increasing interests in the relation between

2   particulate matter (PM) pollution and atmospheric boundary layer (ABL) structure.

3   This study aimed to qualitatively assess the interaction between PM and ABL

4   structure in essence and further quantitatively estimate aerosol radiative forcing

5   (ARF) effects on the ABL structure. Multi-period comparative analysis indicated that

6   the key to determining whether the haze outbreak or dissipation occurs is whether the

7   ABL structure satisfies the relevant conditions. However, the ABL structure change was

8   in turn highly related to the PM level and ARF. |SFC-ATM| (SFC and ATM are the

9   ARFs at the surface and interior of the atmospheric column, respectively) is the absolute

10   difference between ground and atmosphere layer ARFs, and the |SFC-ATM| change is

11   linearly related to the PM concentrations. However, the influence of ARF on the

12   boundary layer structure is nonlinear. With increasing |SFC-ATM|, the TKE level

13   exponentially decreased, which was notable in the lower layers/ABL but disappeared

14   at high altitudes/above the ABL. Moreover, the ARF effects threshold on the ABL

15   structure was determined for the first time, namely, once |SFC-ATM| exceeded ~ 55

16   W m^{-2}, the ABL structure tends to quickly stabilize and thereafter change little with

17   increasing ARF. The threshold of the ARF effects on the boundary layer structure

18   could provide useful information for relevant atmospheric environment improvement

19   measures and policies, such as formulating phased air pollution control objectives.

1. Introduction

Most urban agglomerations in China, such as the North China Plain (NCP), have suffered from poor air quality due to rapid increase in anthropogenic emissions. Beijing, as the capital city of China and the principal city in the NCP area, has frequently experienced severe and persistent haze events (Li et al., 2020; Wang et al., 2018; Xu et al., 2019; Zhong et al., 2018). Previous studies have found that the occurrence of PM pollution events in Beijing is not only inseparable from the serious primary emissions and fast formation of secondary aerosols (An et al., 2019; Guo et al., 2014; Li et al., 2017; Wang et al., 2014; Zheng et al., 2015; Wang et al., 2012), but also largely affected by the ABL structure, which controls the diffusion, transmission, and accumulation of pollutants (Han et al., 2009; Kotthaus and Grimmond, 2018; Zheng et al., 2017). For instance, the PM concentration has a strong relationship with the ABL height (ABLH) that determines the volume available for pollutant dispersion (Haman et al., 2014; Schaefer et al., 2009; Su et al., 2018; Tang et al., 2016). In most instances, heavy air pollution episodes occurred with persistent temperature inversions (Xu et al., 2019; Zhong et al., 2017). Weak/calm winds are essential in the long-term increase in air pollutants (Niu et al., 2010; Yang et al., 2016). Additionally, severe air pollution is ever reported positively related to high atmospheric humidity, one of the manifestations of stagnant ABL conditions (Tie et al., 2017; Petäjä et al., 2016). Moreover, the feedback mechanism between the boundary layer structure and aerosol loading during severe pollution events contributing to the outbreak of haze pollution has been presented in previous studies (Huang et al., 2018; Liu et al., 2018;

3

42   Petäjä et al., 2016; Zhong et al., 2018b; Zhong et al., 2019; Zhao et al., 2019).

43   However, this topic has yet to be fully understood. More work is needed to

44   systematically study the interaction between ABL structure and PM pollution. Since

45   the surface directly influences the ABL, it is the only atmosphere layer characterized

46   by turbulent activities, while higher atmosphere layers are weakly turbulent because

47   of the strongly stable stratification (Munro, 2005). The ABL acts as a notable

48   turbulence buffer coupling the surface with the free atmosphere, and PM and gas

49   pollutants mainly suspended in the ABL are convectively spread throughout it. The

50   change of boundary layer structure determining the accumulation and diffusion of

51   pollutants in it could be largely linked to the difference of turbulent activity (Garratt et

52   al., 1992). Moreover, the change in solar radiation reaching the ground drives the

53   diurnal ABL evolution (Andrews, 2000). While the diurnal evolution of the

54   atmospheric thermodynamic status could be greatly affected considering a strong

55   aerosol direct radiation effect, namely strongly scattering radiation and absorbing

56   radiation (Dickerson et al., 1997; Liu et al., 2018; Huang et al., 2018; Stone et al.,

57   2008; Zhong et al., 2018a). As previous studies have reported that aerosol absorption

58   and scattering effects during severe air pollution notably enhance atmospheric

59   stability and suppress the boundary layer development (Barbaro et al., 2014; Ding et

60   al., 2016; Wilcox et al., 2016; Yu et al., 2002). Considering the aerosol radiative

61   forcing (ARF) is a critical parameter to quantify the aerosol direct radiation effect

62   (Gong et al., 2014; Li et al., 2018). The influence degree of ARF on the boundary

63   layer structure is still unclear, and thus quantitatively determining the effects of ARF

64   on the ABL structure is urgently needed.

65   In this study, we systematically analyzed the way the ABL interacts with PM

66   pollution via contrastive analysis of multiple haze episodes, based on not only specific

67   meteorological factors but also turbulent activity profiles and atmospheric stability

68   indicators. Meanwhile, taking the turbulent kinetic energy (TKE) and ARF as

69   important parameters, we further investigated the influence degree of the aerosol

70   direct radiation effect on the boundary layer structure. Besides, this paper analyzed

71   the interaction between the ABL structure and air pollution using high-resolution and

72   real-observation datasets, such as temperature and humidity profiles of microwave

73   radiometers, horizontal and vertical wind vector profiles of Doppler wind lidar,

74   ABLH, and aerosol backscattering coefficient profiles of ceilometers. Wind profile

75   lidar and microwave radiometers have the advantage of providing direct and

76   continuous observations of the boundary layer over long periods and can characterize

77   the ABL structure up to 2-3 km (Pichugina et al., 2019; Zhao et al., 2019),

78   compensating for the deficiencies of previous research.

79   **2. Data and methods**

80   Figure S1 shows the observation site of the Tower Branch of the Institute of

81   Atmospheric Physics (IAP), Chinese Academy of Sciences (39°58'N, 116°22'E;

82   altitude: 58 m) in Beijing and the sampling instruments in this study. The IAP site is a

83   typical urban Beijing site, and all the sampling instruments are placed at the same

84   location, and simultaneous monitoring is conducted. We conducted a two-month

85   measurement campaign of the PM concentration and aerosol optical depth (AOD) and

obtained vertical profiles of atmospheric parameters such as temperature, humidity,

wind vectors, atmospheric stability, and turbulent activity to better understand how

the boundary layer structure responds to the aerosol direct radiation effect.

The algorithm of SBDART (Santa Barbara DISORT Atmospheric Radiative

Transfer) (Levy et al., 2007) is the core model to calculate the aerosol radiative

forcing parameters. More information on the input parameters of SBDART were

presented in Table S2. A standard mid-latitude atmosphere is used in SBDART in

Beijing. AOD and Ångström Exponent (AE) at 550 nm were obtained from a sun-

photometer. Multiple sets of Single Scattering Albedo (SSA) and backscattering

coefficient were calculated based on MIE theory, and surface albedo & path radiation

were read from MODIS (MOD04), which is used to calculate radiative forcing at the

top of atmosphere (TOA). The TOA results were combined with MODIS

observations, and the result which has the lowest deviation are defined as the actual

parameters of aerosols, and this set of parameters would be used to calculate the

radiative forcing at the surface, top, and interior of the atmospheric column (Gong et

al., 2014; Lee et al, 2018; Xin et al., 2016). Hourly radiative forcing parameters,

including the ARF at the top, surface (SFC), and interior of the atmospheric column

(ATM) at an observation site in Beijing can be calculated based on this algorithm.

More detailed descriptions are provided in our previous work (Gong et al., 2014; Lee

et al, 2018; Xin et al., 2016).

Air temperature and relative and absolute humidity profiles were retrieved with a

microwave radiometer (after this referred to as MWR) (RPG-HATPRO-G5 0030109,

Germany). The MWR produces profiles with a resolution ranging from 10-30 m up to

0.5 km, profiles with a resolution ranging from 40-70 m between 0.5 and 2.5 km, and

profiles with a resolution ranging from 100-200 m from 2 to 10 km at a temporal

resolution of 1 s. More detailed information on the RPG-HATPRO-type instrument

can be found at http://www.radiometer-physics.de (last access: 4 June 2020).

Vertical wind speed and horizontal wind vector profiles were obtained by a 3D

Doppler wind lidar (Windcube 100s, Leosphere, France). The wind measurement

results have a spatial resolution ranging from 1-20 m up to 0.3 km and a spatial

resolution of 25 m from 0.3 to 3 km, at a temporal resolution of 5 s. More instrument

details can be found at www.leosphere.com (last access: 4 June 2020).

A ceilometer (CL51, Vaisala, Finland) was adopted to acquire atmospheric

backscattering coefficient (BSC) profiles. The CL51 ceilometer digitally receives the

return backscattering signal from 0 to 100 μs and provides BSC profiles with a spatial

resolution of 10 m from the ground to a height of 15 km. The ABLH was further

identified by the sharp change in the BSC profile's negative gradient (Münkel et al.,

2007), and detailed information is reported in previous studies (Tang et al., 2015,

2016; Zhu et al., 2018).

A CIMEL sun-photometer (CE318, France), a multichannel, automatic sun-and-

sky scanning radiometer (Gregory, 2011), was used to observe the AOD, and the AOD

at 500 nm is adopted in this paper. The real-time hourly mean ground levels of $PM_{2.5}$

(particulate matter with aerodynamic diameter less than or equal to 2.5 μm) and PM_{10}

(particulate matter with aerodynamic diameter less than or equal to 10 μm) were

130   downloaded from the China National Environmental Monitoring Center (CNEMC)

131   (available at http://106.37.208.233:20035/, last access: 4 June 2020).

132   More atmospheric parameters regarding the boundary layer structure used in this

133   study are introduced in S1.

134   **3. Results and discussion**

135   **3.1. General haze episodes over Beijing in winter**

136   It is well known that severe air pollution episodes frequently occur in Beijing

137   during winter (Jin-Xiang, 2007; Zhang et al., 2017). Two-month PM concentration

138   data from Beijing in the winter of 2018 were collected. As expected, during this time,

139   Beijing experienced severe and frequent haze pollution episodes with two heavy

140   episodes in which the maximum hourly $PM_{2.5}$ concentration reached ~200 $\mu g\ m^{-3}$ and

141   six moderate episodes in which the $PM_{2.5}$ mass concentration ranged from ~100-150

142     $\mu g\ m^{-3}$ (Figure S2a).

143   Although the air pollution process is variable and complicated, it is worth stating

144   that Beijing's haze pollution in winter can be generally classified as two kinds of

145   patterns, as shown in Figure S2b. For all haze episodes ①-⑦, the $PM_{2.5}$ mass

146   concentration slowly increased in the afternoon of the 1st day, followed by a

147   secondary maximum in the early morning and a maximum at midnight of the 2nd day.

148   In comparison to the processes of ④-⑦, where the $PM_{2.5}$ mass concentration sharply

149   decreased to <25 $\mu g\ m^{-3}$ in the early morning of the 3rd day, during periods ①-③,

150   however, the highest $PM_{2.5}$ mass concentration (~100-200 $\mu g\ m^{-3}$) was observed on

151   the whole 3rd day, which disappeared on the 4th day. As previously reported,

transport, chemical transformation and boundary layer structure (local meteorological

conditions) are central to determining the amount and type of pollutant loading.

Considering the equivalent emission and transport effects, the suspended particles in

④-⑦ subjected to diffuse would be controlled by the atmospheric motion (wind and

turbulence) on the 3rd day. The particles during periods ①-③ continuing to

accumulate were therefore highly related to the specific ABL status. To investigate the

possible reasons for the different variation trends of haze episodes ①-③ and ④-⑦,

in the next section, we will mainly focus on the ABL structure (local meteorological

conditions) influences.

3.2. Qualitative analysis of the interaction between particulate matter and boundary layer structure
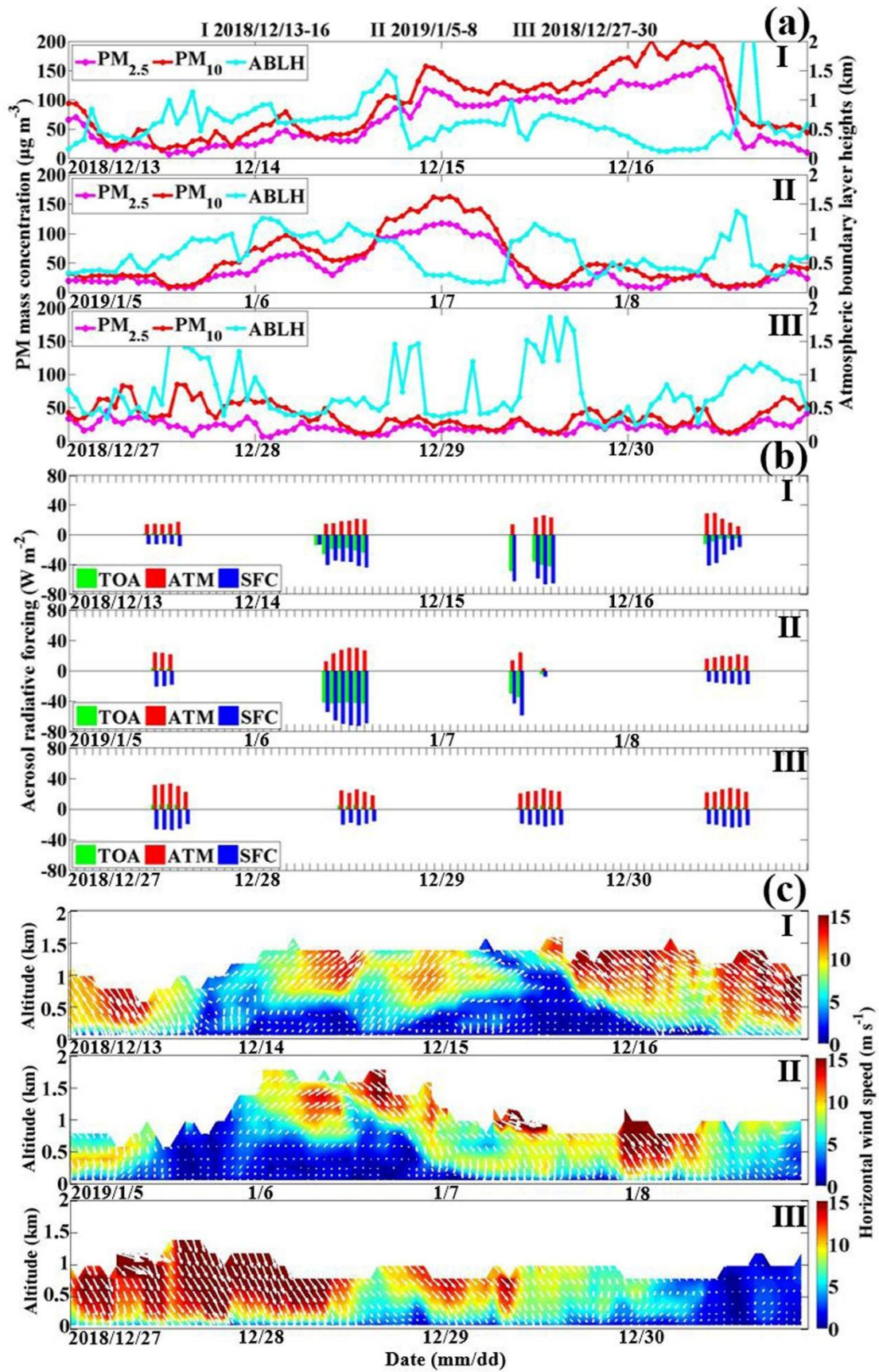
Figure 1. Temporal evolution of (a) the PM mass concentration and atmospheric

164   boundary layer height (PM$_{2.5}$: solid pink lines; PM$_{10}$: solid red lines; ABLH: solid

165   blue lines), (b) aerosol radiative forcing at the top (TOA; green bars), surface (SFC;

166   blue bars) and interior of the atmospheric column (ATM; red bars), and (c) horizontal

167   wind vector profiles (shaded colors: wind speeds; white arrows: wind vectors) during

168   the typical haze pollution episodes of I (2018/12/13-16) and II (2019/1/5-8) as well as

169   the typical clean period of III (2018/12/27-30).
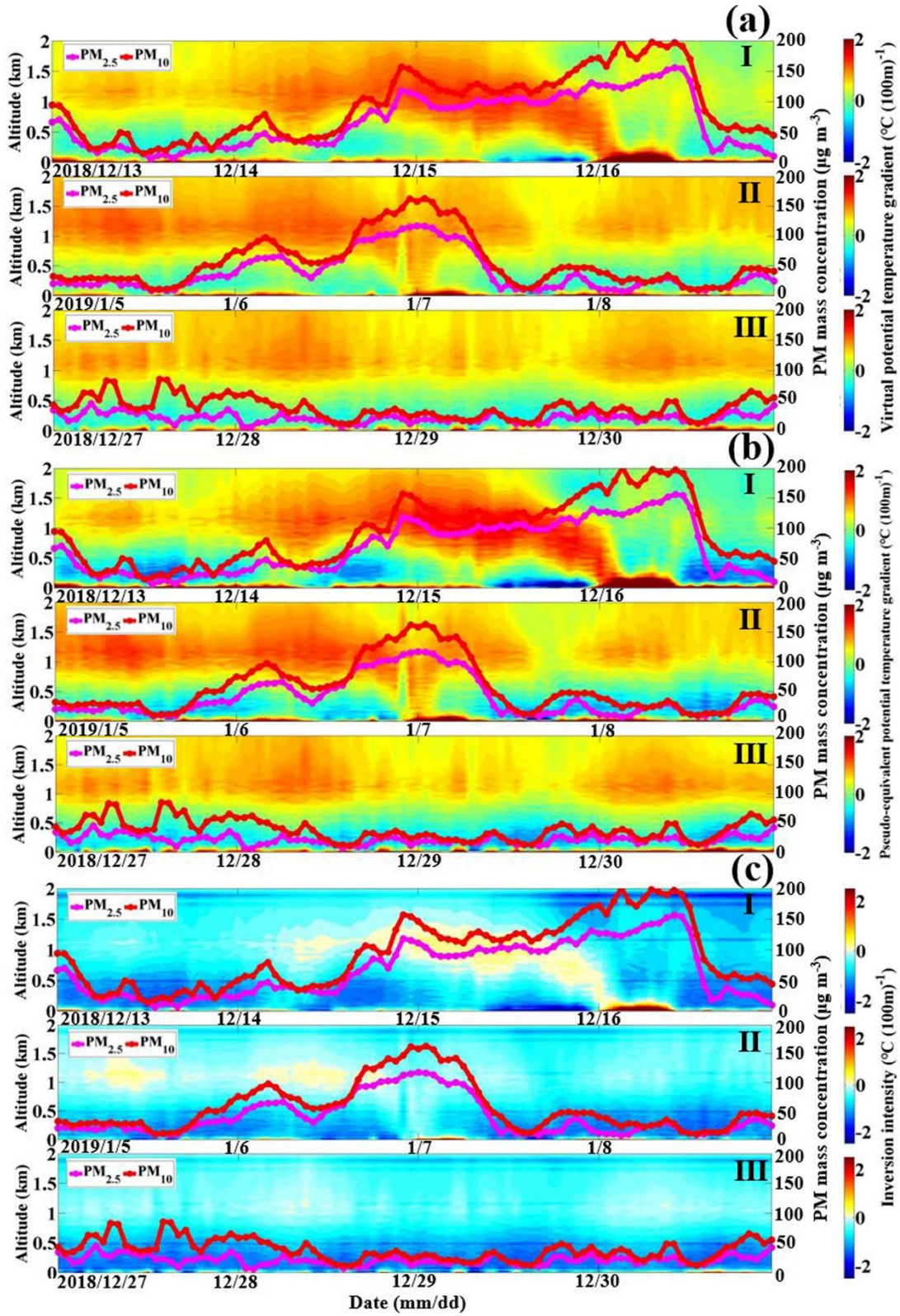
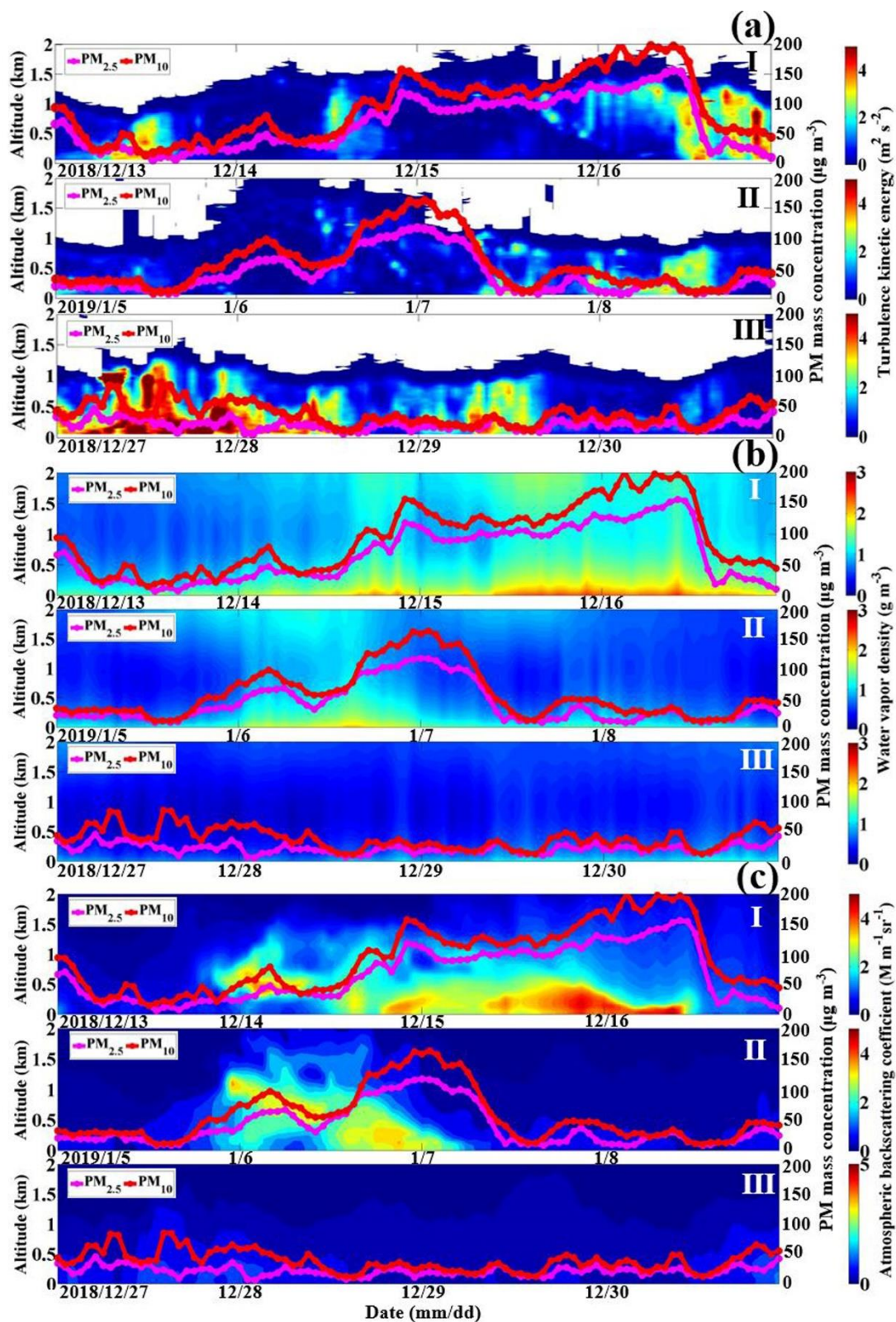Figure 2. Temporal variation in the vertical profiles of (a) the virtual potential

temperature gradient ($\partial\theta v/\partial z$), (b) pseudoequivalent potential temperature gradient

($\partial\theta se/\partial z$) and (c) temperature inversion phenomenon (shaded colors: inversion

174   intensity) during the typical haze pollution episodes of I (2018/12/13-16) and II

175   (2019/1/5-8) as well as the typical clean period of III (2018/12/27-30).

176

177   Figure 3. Temporal variation in the vertical profiles of (a) the turbulent activity

178 (shaded colors: TKE), (b) atmospheric humidity (shaded colors: vapor density), and

179 (c) vertical distribution of suspended particles (shaded colors: BSC) during the typical

180 haze pollution episodes of I (2018/12/13-16) and II (2019/1/5-8) as well as the typical

181 clean period of III (2018/12/27-30).

182   The haze episodes in winter in Beijing basically followed two different kinds of

183 variation patterns as described in the previous section. The specific reason for this

184 finding will be systematically analyzed in this section. To better illustrate the two

185 different haze patterns, a typical clean period will be considered a control. The typical

186 air pollution episodes I (E-I) (13-16 December 2018) and II (E-II) (5-8 January 2019),

187 as well as the typical clean episode III (E-III) (27-30 December 2018), are chosen as

188 examples for analysis.

189   *a. Similar change trends in the first two days*

190   Numerous studies have reported that PM's original explosive growth is caused

191 by pollution transport under southerly winds (Ma et al., 2017; Zhao et al., 2019;

192 Zhong et al., 2018). In this study, the action of southerly winds on the air pollution in

193 Beijing was presented more clearly as the Windcube 100s lidar obtained the

194 distribution of the horizontal wind vectors extending to heights of 1-1.5 km

195 (equivalent to the entire ABL) (Figure 1c). On the 1st day of E-I and E-II, the

196 atmosphere layer up to ~1 km in height was controlled by strong and clean north

197 winds, exactly like clean E-III. No pollution transport occurred, and the PM and ARF

198 levels were equivalent to those on a clean day (Figures 1a-b). The atmospheric

199 backscattering coefficients throughout the ABL during the three episodes only ranged

14

200 from ~0-1.5 M m^{-1} sr^{-1} (Figure 3c). From the evening of the 1st day to the forenoon of

201 the 2nd day, strong southerly winds blew across Beijing during both E-I and E-II, with

202 the wind speed reaching ~5-15 m s^{-1} at an atmosphere of about 0.5-1.5 km, while

203 north winds still dominated the ABL during clean E-III. Sensitive to the change in

204 wind direction from north to south, the PM concentration progressively increased

205 from a fairly low level to ~50 μg m^{-3}. Moreover, the BSCs sharply increased to ~3

206 Mm^{-1} rd^{-1} and were concentrated at altitudes from ~0.5-1 km, which further stressed

207 the effects of southerly transport on the PM concentration's original growth over

208 Beijing. With prevailing winds originating from the wetter south, compared to the low

209 humidity during clean E-III, the air humidity in Beijing during this time also

210 increased, with the vapor density ranging from ~1.5-2 g m^{-3} for both E-I and E-II

211 (Figure 3b).

212   At midnight of the 2nd day, the PM concentration reached its highest level with a

213 PM$_{2.5}$ (PM$_{10}$) concentration of ~110 (150) μg m^{-3} during both E-I and E-II.

214 Meanwhile, the highest BSC values mainly occurred from the ground to a height of 1

215 km at this time, implying that a portion of the suspended particles was pushed down

216 to the near-surface. Before southerly wind transport occurred, the evolution of the

217 stability indicator ($\partial\theta_v/\partial z$; $\partial\theta_{se}/\partial z$) profiles during E-I and E-II was analogous to that

218 during clean E-III (Figures 2a-b). The stratification states at the different heights (0-1

219 km) were either unstable or neutral, with negative or zero $\partial\theta_v/\partial z$ values, respectively,

220 whereby no clear nor strong temperature inversion phenomenon occurred in the

221 boundary layer (Figure 2c). And the corresponding ABLHs were the same (Figure 1a).

222   However, the atmospheric stratification from ~0.5-1 km during E-I and from 0-1 km

223   during E-II became quite stable at night of the 2nd day, with positive values of $\partial\theta_{se}/\partial z$

224   and weak turbulent activity (TKE: ~0 m^2 s^{-2}) (Figure 3a). In contrast to an increased

225   ABLH during clean E-III, the ABLHs during E-I and E-II sharply decreased.

226   Considering strong aerosol scattering and absorbing radiation could affect the

227   temperature stratification (Li et al., 2010; Zhong et al., 2018a). With the elevated PM

228   level due to southerly transport during E-I and E-II, ARF increased as expected with

229   SFC (ATM) reaching ~-40 (~20) W m^{-2} and ~-75 (~30) W m^{-2}, respectively. Besides,

230   TOA has an analogous variation trend with SFC, increasing from relatively low

231   values to ~-20 W m^{-2} and ~-45 W m^{-2}, respectively. Therefore, less radiation reached

232   the ground and more heated the atmosphere above the ground during E-I and E-II, and

233   in comparisons with clean E-III, the atmospheric stratification was altered and the

234   stability was thus increased at night. The suspended particles brought by southerly

235   transport originally occurring at high altitudes were restrained from vertically

236   spreading and gradually sank due to gravity and accumulated near the surface.

237   *b.   Different change trends in the next two days*

238   It is salient to note that the haze evolution trends during E-I and E-II were

239   consistent so far, corresponding to a similar ABL structure. Nevertheless, the north

240   winds (~10-15 m s^{-1}) during E-II, which only blew above the ABL (>1 km) at

241   midnight of the 2nd day, gradually spread downward and controlled the whole

242   boundary layer on the 3rd day. The wind field is critical concerning horizontal

243   dispersion in the boundary layer; thus, the strong, clean and dry north winds during E-

II greatly diffused the already accumulated particles first, where the $PM_{2.5}$ mass

concentration decreased from ~100 to ~50 µg m^{-3}. The ARF obtained at 9:00 sharply

decreased compared to yesterday, and with solar radiation heating the ground in the

morning on the 3rd day, the development of daytime mixing layer eliminated the

previous night's temperature structure. The temperature stratification became similar

to that on clean E-III with a similar increase in ABLH. An unstable/neutral

atmospheric state with a TKE of ~2 m^2 s^{-2} was also conducive to the vertical spread of

substances. In response, the PM concentration (BSC) and air humidity during E-II

gradually decreased with the convective boundary layer development and reached the

same level as those during clean E-III.

Different from E-II, in which clean and strong north winds in the 3rd daytime

contributed to the diffusion of previous night's stable stratification, there were still

south winds in E-I, which once filled the boundary layer on the 2nd day, gradually

decelerated over time from the ground to high altitudes. The atmosphere layer with

calm/light winds extended from the ground to the height of ~1.0 km in the 3rd

daytime and gradually down to the height of ~0.2 km at midnight and the forenoon of

the 4th day. Due to the maintaining high PM levels, SFC and TOA further increased,

up to ~-40 W m^{-2} and ~-75 W m^{-2}, respectively, with ATM remaining high (~25 W m^{-2}), which facilitated the temperature inversion that lasted from the whole 3rd day to

the noon of the 4th day. As shown in Figure 2(a-c)-I, there was continue temperature

inversion structure from ~0.5-1.0 km altitude and the atmospheric stratification was

quite stable on the 3rd daytime and at midnight. Since the temperature inversion layer

266   acted as a lid at altitudes of ~0.5-1.0 km, downward momentum transport would be

267   blocked. Original south winds near the ground were constantly consumed by friction,

268   further explaining the lower atmosphere layer's calm/light winds. With quite strong

269   north winds started blowing at high altitude at the 3rd night and surface cooling

270   strengthening, the temperature inversion at ~0.5-1.0 km was gradually broke and

271   turned to ground-touching temperature inversion at 0-0.2 km altitude at midnight.

272   This abnormal temperature structure lasted till noon of the 4th day, mainly due to the

273   strong aerosol direct radiation effect of the pre-existing high PM level. As expected,

274   we can see the strong north winds above ~1.0 km at the 3rd night gradually extended

275   downward and eventually occurred above the ground-touching inversion in the

276   forenoon of the 4th day. Therefore, with calm/light winds and weak turbulent activity

277   below the temperature inversion in the 3rd day, the PM concentrated exactly below

278   the inversion lid (below ~0.5 km) and maintained high concentrations, as the BSC

279   distribution shows in Figure 3c-I. With strong ground-touching inversion of 0-0.2 km

280   altitude forming at midnight and the forenoon of the 4th day, the accumulated

281   particles near the surface were further inhibited right in the stable atmosphere layer

282   (below ~0.2 km). The same effect was exerted on the water vapor so as to the high air

283   humidity below the inversion lid at this time. Therefore, the pollutant layer was

284   compressed downward accompanied by intense heterogeneous hydrolysis reactions at

285   the moist particle surface (Zhang et al., 2008), thus resulting in the continue increase

286   of near-surface $PM_{2.5}$ concentrations. At noon of the 4th day, the north winds further

287   accelerated with wind speed higher than ~15 m s^{-1} and spread down to the whole

ABL, which promoted the horizontal and convective dispersion of pollutants and water vapor, and the PM mass concentration, therefore, dropped to the same level as that on clean E-III. With $PM_{2.5}$ sharply dropped from ~150 μg m^{-3} to ~20 μg m^{-3} in four hours, the aerosol direct radiation effect was sensitive to PM changes and gradually decreased from 10:00 to 14:00, reaching the same level as those on clean E-III finally.

In this section, through a detailed contrastive analysis, we examined the potential reasons for the occurrence of the two different patterns of haze pollution in winter in Beijing. We found that the crucial point in determining whether the PM mass concentration remained high or sharply decreased was related to whether the boundary layer remained stable. The boundary layer stability was, in turn notably linked to the PM mass concentration and aerosol direct radiation effect.

**3.3. Quantitative analysis of the effect of particulate matter on the boundary layer structure**
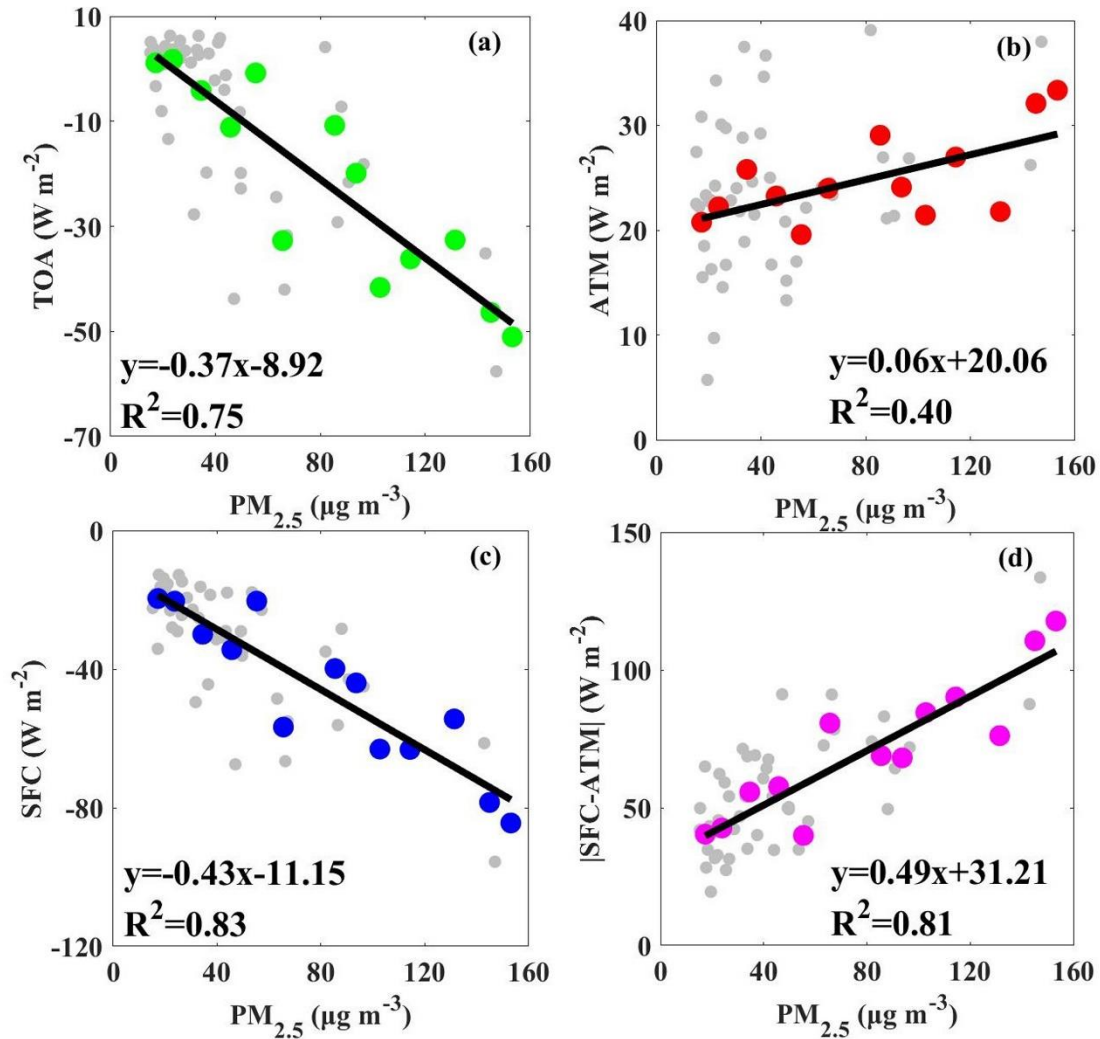
Figure 4. Scatter plots of the $PM_{2.5}$ mass concentration (x) versus aerosol radiative

forcing at the top of the atmospheric column (TOA; y; a), the interior of the

atmospheric column (ATM; y; b), and the surface (SFC; y; c) as well as the absolute

difference of SFC and ATM (|SFC-ATM|; y; d), respectively (gray dots: daily data;

other dots: mean data). (The daily data means daily mean values of TOA, ATM, SFC,

and corresponding daily averaged $PM_{2.5}$ mass concentration from 27 November 2018

to 25 January 2019 in Beijing. The mean $PM_{2.5}$ concentrations were obtained by

averaging daily $PM_{2.5}$ concentrations at intervals of 10 μg m^{-3}. The mean TOA, ATM,

and SFC were obtained after the corresponding daily TOA, ATM, and SFC average,

312   respectively. For example, all daily PM$_{2.5}$ concentrations greater than 40 µg m^{-3} and

313   less than 50 µg m^{-3} were averaged as a mean PM$_{2.5}$ concentration, and TOA values

314   (ATM; SFC) corresponding to this daily PM$_{2.5}$ concentration range were also averaged

315   as a mean TOA (ATM; SFC)).
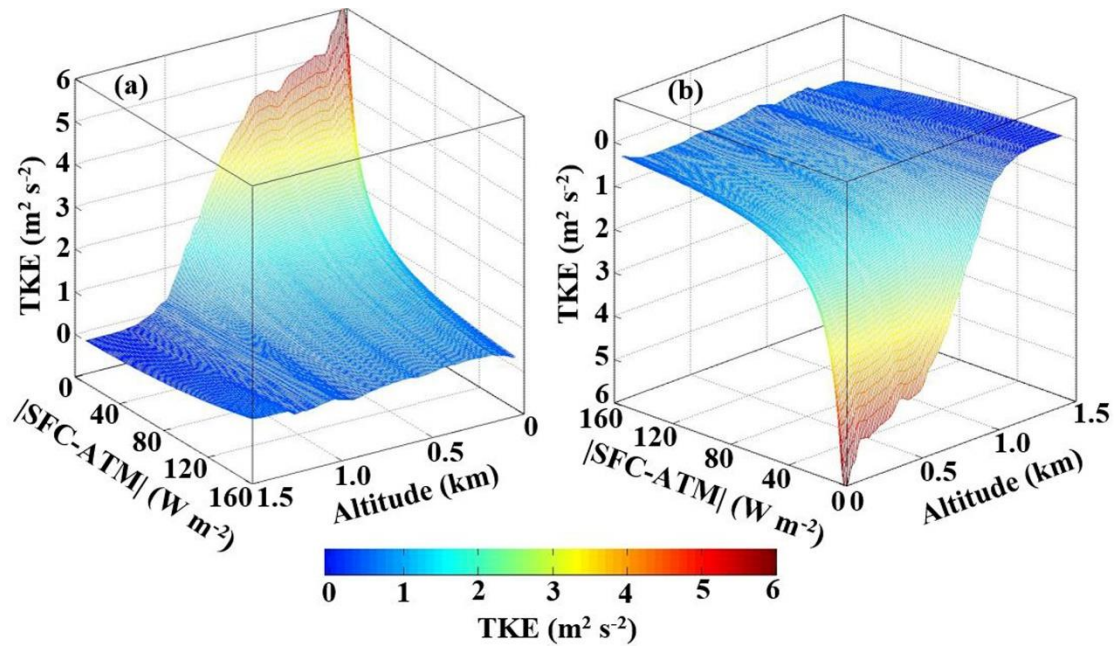
316

317   Figure 5. 3-D plot of the fitting relationship of the absolute difference in aerosol

318   radiative forcing between the surface and interior of the atmospheric column (|SFC-

319   ATM|; *x*) and turbulence kinetic energy (TKE; *z*) at the different altitudes (*y*) ((a) and

320   (b) present different perspectives).
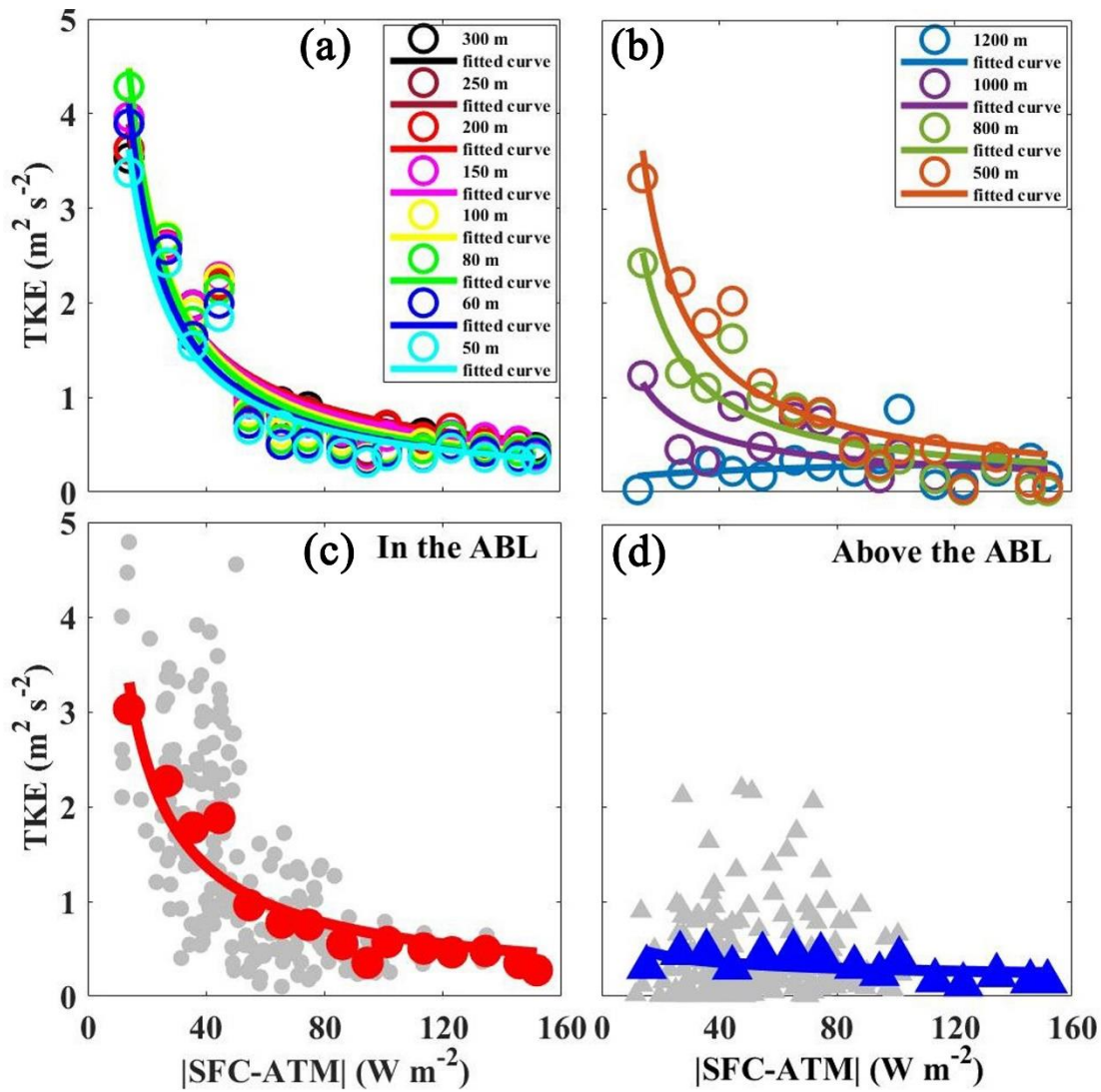
Figure 6. Scatter plots of the mean absolute difference of the aerosol radiative forcing at the surface and interior of the atmospheric column (|SFC-ATM|; x) versus the mean turbulence kinetic energy (TKE; y) at the different altitudes (a; b). Scatter plots of |SFC-ATM| (x) versus TKE (y) in the ABL (c) and above the ABL (d) (gray dots: hourly data; other dots: mean data). The hourly data were collected over a two-month period in Beijing from 27 November 2018 to 25 January 2019. (The hourly data means hourly mean values of |SFC-ATM| and corresponding hourly TKE. The mean |SFC-ATM| was obtained by averaging hourly |SFC-ATM| at intervals of 10 W m^{-2}, then the mean TKE was obtained after the average of the corresponding hourly TKE.).
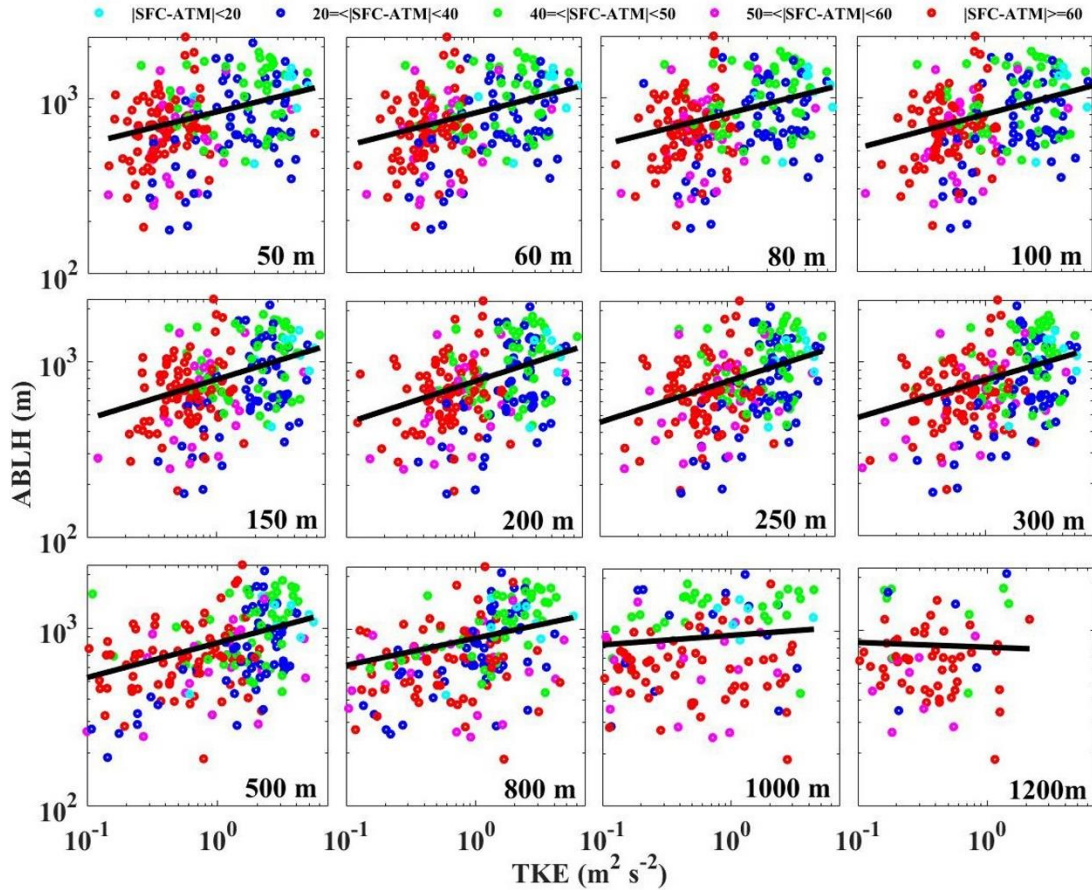
Figure 7. The atmospheric boundary layer height (ABLH; y) as a function of the turbulence kinetic energy (TKE; x) at the different altitudes and the aerosol direct radiation effect defined as |SFC-ATM| (color code). The calculated hourly data used above are collected over two months in Beijing from 27 November 2018 to 25 January 2019.

Based on the contrastive analysis in the previous section, it was clear that the ABL structure played a critical role in the maintenance and dissipation of air pollution. It appeared that the increase in atmospheric stability suppressed pollution diffusion under a weak turbulence activity and low ABLH. Water vapor also significantly accumulated to a relatively high level near the surface, further facilitating secondary aerosols' formation. The evolution of ABL stability essentially

343 occurred in response to the atmospheric temperature structure, as analyzed above,

344 which was influenced by the strong aerosol direct radiation effect (Andrews, 2000; Li

345 et al., 2010). The Archimedes buoyancy generated by the pulsating temperature field

346 in the gravity field exerted negative work on the turbulent pulsating field with a stable

347 ABL occurring. The turbulence served as a carrier for substance transport in the

348 boundary layer, such as water vapor, heat, and PM (Garratt et al., 1992). Thus, in the

349 following section, the ARF and TKE were chosen as the key parameters to examine

350 how PM affects and modifies the boundary layer structure.

351   Figure 4 shows the relationship between the PM concentration and ARF. As

352 shown in Figures 4a and 4c, TOA and SFC were proportional to the $PM_{2.5}$

353 concentration, respectively. With the increase in $PM_{2.5}$ concentration, elevated aerosol

354 loading near the surface would scatter more solar radiation back into outer space and

355 cause less solar radiation reaching the ground, corresponding to a cooling of the

356 surface and making negative SFC. TOA means the aerosol radiative forcing at the top

357 of the atmosphere column and is the sum of ATM and SFC. Considering that

358 anthropogenic aerosols are mostly scattering aerosols, the SFC forcing is generally

359 stronger than ATM, corresponding to a cooling of the earth-atmosphere system. The

360 TOA forcing was thus usually negative and had a similar trend with SFC. ATM,

361 driven by aerosol absorption effect and representing a warming effect of aerosols on

362 the atmosphere layer, exhibited a positive correlation with the $PM_{2.5}$ concentration

363 (see Figure 4b). These results demonstrated that a higher $PM_{2.5}$ concentration would

364 arouse a stronger ARF, further inhibiting solar radiation from reaching the ground and

heating the atmosphere layer more. |SFC-ATM|, defined as the absolute value of the

difference between SFC and ATM, represents aerosols' combined action on the solar

radiation reaching the aerosol layer and the ground. Larger values of |SFC-ATM|

indicate stronger aerosol scattering and/or absorption effects, further implying a more

significant temperature difference between the ground and the above atmosphere

layer. As expected, a positive linear correlation between |SFC-ATM| and $PM_{2.5}$

concentration was found, as shown in Figure 4d.

As described in the above paragraph, there was a strong ARF under a high PM

loading, which markedly altered the atmospheric temperature structure, further

changing the ABL structure. It is necessary to determine the effect degree of ARF on

the boundary layer structure. Figure 5 shows the 3-D plots of the fitting relationship

between the hourly values of |SFC-ATM| and TKE at the different altitudes. What

stood out in Figure 5a was the general decline in TKE concerning the growth of |SFC-

ATM|. With increasing |SFC-ATM| value, the TKE value at the different altitudes

always decreased exponentially and approached zero below ~0.8 km. The notable

exponential function between TKE and |SFC-ATM| explained that a strong ARF

would drastically change the boundary layer into highly stable conditions

characterized by a rather low TKE. The results above highlight the aerosol direct

radiation effect's nonnegligible impact on the boundary layer structure, especially

during the haze episode under a high aerosol loading with a strong ARF. It is well

known that a larger net negative/positive SFC/ATM arises a cooler/warmer

ground/atmosphere. An increase in |SFC-ATM| implies the gradual intensification of

387 the ground cooling and/or atmosphere heating processes. Therefore, it changed the

388 atmospheric stratification into a gradually enhanced stable state, which was

389 characterized by increasingly weaker turbulence activities. Additionally, as shown in

390 Figure 5b, we can identify a critical point of the |SFC-ATM| effects on TKE in the low

391 layers. In particular, TKE decreased with increasing |SFC-ATM| and hardly changed

392 when |SFC-ATM| exceeded the critical point.

393   To define the critical point, we generated scatter plots of the average |SFC-ATM|

394 and TKE at different altitudes, as shown in Figures 6a-b. The scatter plots of the

395 unaveraged hourly data are shown in Figure S3, and the fitting functions are listed in

396 Table S1. Depending on the exponential curve's maximum curvature (Silvanus and

397 Gardner, 1998), a critical point should exist. With the mean TKE and |SFC-ATM|

398 values on the exponential curve, we found that once the aerosol direct radiation effect

399 defined by |SFC-ATM| exceeded 50-60 W m^{-2} (average of ~55 W m^{-2}), the TKE

400 sharply decreased from ~2 m^2 s^{-2} to lower than 1 m^2 s^{-2}. This means that a high aerosol

401 loading with a |SFC-ATM| value higher than ~55 W m^{-2} tends to change the boundary

402 layer from the unstable state to the extremely stable state in a short time, and further

403 increasing |SFC-ATM| would barely modify the ABL structure. The average |SFC-

404 ATM| value of ~55 W m^{-2} can be defined as the threshold of the ARF effects on the

405 ABL structure, which could provide useful information for relevant model

406 simulations, atmospheric environment improvement measures, and relevant policies.

407 Besides, as shown in Figures 5-6, the exponential relationship between TKE and

408 |SFC-ATM| was notable in the low layers and gradually deteriorated with increasing

409 altitude. On average, the exponential relationship was notable in the ABL and almost

410 disappeared above the ABL (Figures 6c-d). Considering that aerosols are mainly

411 concentrated below the lower atmosphere, contributing the most to the SFC and ATM

412 forcing, which further confirmed that the considerable change in atmospheric

413 stratification caused by aerosols existed and mainly occurred in the lower layers.

414　　　The previous discussion shows that a strong aerosol direct radiation effect

415 markedly affected the turbulent activity and modified the boundary layer structure. As

416 many studies have reported, the ABLH is an important meteorological factor that

417 influences the vertical diffusion of atmospheric pollutants and water vapor (Stull,

418 1988; Robert and Aron, 1983). The following examines the relationship among the

419 turbulent activity, ARF, and ABLH to illustrate the change in ABLH in response to

420 ARF. Figure 7 shows the ABLH as a function of the TKE and |SFC-ATM| at the

421 different altitudes. It was apparent that a positive correlation exists between TKE and

422 ABLH. As the turbulent activity became increasingly weaker, the corresponding

423 boundary layer height gradually decreased, responding to the gradual increase in

424 |SFC-ATM|. Similar to the relationship between the turbulent activity and aerosol

425 radiative effect, as shown in Figure 6, the relationship among these aspects was much

426 stronger below 300 m and almost disappeared above 800 m. This further addressed

427 the fact that the change in boundary layer height was attributed to the turbulence

428 activity variation stemming from the aerosol direct radiation effect.

429　　　Thus far, this section has demonstrated that the aerosol loading with aerosol

430 radiative effects impacted the turbulent activity, changed the boundary layer height,

431 and modified the boundary layer structure. On the other hand, it is now necessary to

432 explain how the renewed boundary layer structure modifies the $PM_{2.5}$ concentration.

433 As shown in Figures S4a-b, the ABLH as an independent variable impact the ambient

434 water vapor in the ABL to some degree. There was a steady increase in the ambient

435 humidity with decreasing ABLH, where absolute humidity (AH) and relative

436 humidity (RH) were projected to decrease to ~3 g m^{-3} and ~60%, respectively, with

437 the ABLH decreasing below ~500 m. With the increase in ambient humidity, a marked

438 rise in $PM_{2.5}$ concentration occurred, as shown in Figures S4c-d. Once AH and RH

439 exceeded ~3 g m^{-3} and ~60%, respectively, the $PM_{2.5}$ concentration reached ~100 μg

440 m^{-3}. The results above indicate that with a fairly low boundary layer height, water

441 vapor accumulated near the surface, and particles tended to hygroscopic grow,

442 resulting in secondary aerosol formation in a high-humidity environment, further

443 increasing the $PM_{2.5}$ concentration. As shown in Figure S4e, with the level off of the

444 ABLH, the $PM_{2.5}$ mass concentration increased exponentially and reached a high

445 value. The exponential relationship was similar to that between the ambient humidity

446 and ABLH, which revealed that the explosive growth of the $PM_{2.5}$ concentration

447 under a low ABLH was largely driven by intense secondary aerosol formation and

448 hygroscopic growth at high ambient humidity.
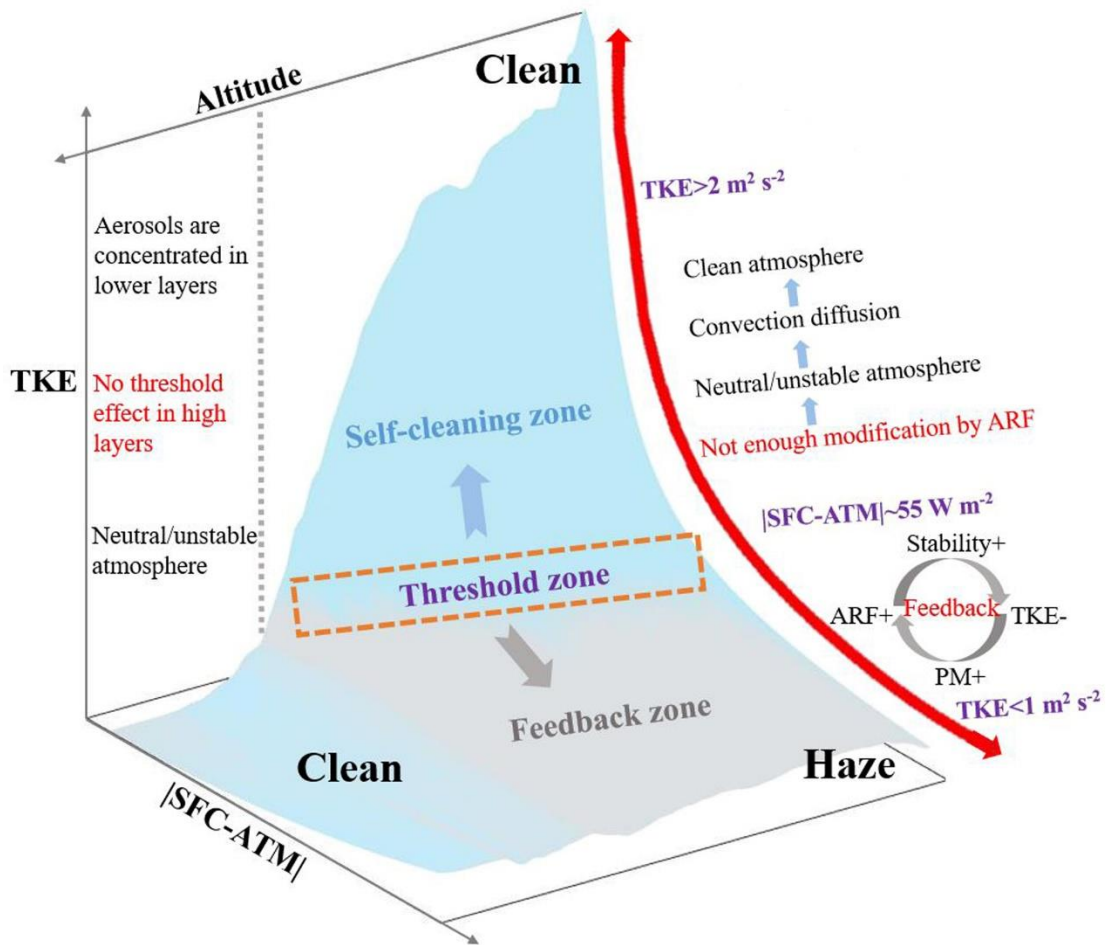
Figure 8. Schematic diagram of the interaction between the aerosol radiative forcing (ARF) and boundary layer structure (|SFC-ATM|: the mean absolute difference of the aerosol radiative forcing at the surface and interior of the atmospheric column; TKE: the mean turbulence kinetic energy).

4. Conclusion

By analyzing the two-month haze conditions in winter in Beijing, we found that haze pollution basically underwent two different variation patterns, namely, the same trends on the first two days, and on the next days, one haze pattern went through a continuing outbreak, while the other haze pattern exhibited notable diffusion. Considering equivalent emissions, this has raised important questions about whether and how the local boundary layer structure impacted/caused this difference. The

461 results of a contrastive analysis qualitatively showed that the crucial point in

462 determining whether the PM concentration remained very high or sharply decreased

463 was largely related to whether the boundary layer structure (i.e., stability and TKE)

464 satisfied relevant conditions. As previous studies reported (Liu et al., 2018; Zhong et

465 al., 2018b; Zhong et al., 2019) and was confirmed in this paper, the extremely stable

466 stratification with positive $\partial\theta_{se}/\partial z$ values and a low TKE was the premise of the

467 outbreak of haze pollution. However, the change/state of the boundary layer structure

468 was, in turn, strongly linked to the PM mass concentration and ARF, and we further

469 quantitatively evaluated the effect of ARF on the boundary layer structure. Figure 8,

470 emerging from the previous observation analysis, is where ARF modifies the

471 boundary layer structure and aggravates haze pollution. The ARF effects on the

472 atmospheric stratification depend on the reduced radiation reaching the ground due to

473 aerosol scattering and absorbing radiation in the atmosphere (Dickerson et al., 1997;

474 Stone et al., 2008). Firstly, we found that a positive linear relationship between |SFC-

475 ATM| and $PM_{2.5}$ concentration existed, which means the strong aerosol scattering

476 and/or absorption effect occurs during the heavy haze episodes and could arouse

477 significant temperature differences between the surface and the above atmosphere

478 layer. Secondly, previous studies revealed that black carbon solar absorption

479 suppresses turbulence near the surface (Wilcox et al., 2016); while we found that the

480 TKE value at the different altitudes always decreased exponentially with increasing

481 |SFC-ATM|, which was significant in the lower atmosphere layer. Moreover, the ARF

482 effects on turbulent activity were found significant in the boundary layer and

483 disappeared above the boundary layer, which also confirmed that the stronger ARF

484 from the aerosol layer would indeed change the boundary layer into the considerably

485 stable state characterized by a relatively low TKE. Thirdly, the ARF change is linear

486 due to the PM concentration; however, the influence of ARF on the boundary layer

487 structure is nonlinear. Based on the exponential relationship, the threshold of the ARF

488 effects on the boundary layer structure has been determined for the first time,

489 highlighting that once the ARF exceeded a specific value, the boundary layer structure

490 tends to quickly stabilize after that changed little with increasing ARF. This threshold

491 could provide useful information for relevant atmospheric environment improvement

492 measures and policies in Beijing. When the $PM_{2.5}$ concentration is controlled with the

493 ARF below the threshold, the unstable atmosphere's self-purification capacity could

494 effectively dilute and diffuse pollutants. In contrast, when the $PM_{2.5}$ concentration

495 increases with an ARF exceeding the threshold value, the boundary layer would

496 stabilize sharply, especially in the lower layers, aggravating haze pollution.

Data availability

The surface $PM_{2.5}$ & PM_{10} and other trace gases observation data used in this study can

be accessed from http://106.37.208.233:20035/ (last access: 4 June 2020). Other

datasets can be accessed upon request to the corresponding author.

Author contribution

XJ designed the experiments and the research. ZD, GC, QJ, WY, TG, MY, DL, WX,

LG, MY provided experimental assistance and analytical method. ZD and XJ analyzed

the data and performed research. All authors commented on the manuscript.

Competing interests

The authors declare that they have no conflict of interest.

Acknowledgments

References

An, Z., Huang, R.-J., Zhang, R., Tie, X., Li, G., Cao, J., Zhou, W., Shi, Z., Han, Y., Gu, Z., and Ji, Y.: Severe haze in northern China: A synergy of anthropogenic emissions and atmospheric processes, Proc. Natl. Acad. Sci. U. S. A., 116, 8657-8666, https://doi.org/10.1073/pnas.1900125116, 2019.

Andrews, D. G.: An Introduction to Atmospheric Physics, Cambridge University Press, 2000.

Barbaro, E., Arellano, J., Ouwersloot, H., Schröter, J., Donovan, D., and Krol, M.: Aerosols in the convective boundary layer: Shortwave radiation effects on the coupled land‑atmosphere system, J. Geophys. Res.: Atmos., 119, 5845–5863, https://doi.org/10.1002/2013JD021237, 2014.

Dickerson, R. R., Kondragunta, S., Stenchikov, G., Civerolo, K. L., Doddridge, B. G., and Holben, B. N.: The impact of aerosols on solar ultraviolet radiation and photochemical smog, Science (New York, N.Y.), 278, 827-830, https://doi.org/10.1126/science.278.5339.827, 1997.

Garratt, J. R., Dessler, A. J., Houghton, J. T., and Rycroft, M. J.: The atmospheric boundary layer, 1992.

Ding, A., Huang, X., Nie, W., Sun, J., Kerminen, V.-M., Petäjä, T., Su, H., Cheng, Y., Yang, X., Wang, M., Chi, X., Wang, J., Virkkula, A., Guo, W., Yuan, J., Wang, S., Zhang, R., Wu, Y., Song, Y., Zhu, T., Zilitinkevich, S., and Kulmala, M.: Enhanced haze pollution by black carbon in megacities in China, Geophys. Res. Lett., 43, 2873–2879, https://doi.org/10.1002/2016GL067745, 2016.

Gong, C., Xin, J., Wang, S., Wang, Y., Wang, P., Wang, L., and Li, P.: The aerosol direct radiative forcing over the Beijing metropolitan area from 2004 to 2011, J. Aerosol Sci., 69, 62-70, https://doi.org/10.1016/j.jaerosci.2013.12.007, 2014.

Gregory, L.: Cimel Sun-photometer (CSPHOT) Handbook, 2011.

Guo, S., Hu, M., Zamora, M. L., Peng, J., Shang, D., Zheng, J., Du, Z., Wu, Z., Shao, M., Zeng, L., Molina, M. J., and Zhang, R.: Elucidating severe urban haze formation in China, Proc. Natl. Acad. Sci. U. S. A., 111, 17373-17378,

https://doi.org/10.1073/pnas.1419604111, 2014.

Haman, C. L., Couzo, E., Flynn, J. H., Vizuete, W., Heffron, B., and Lefer, B. L.: Relationship between boundary layer heights and growth rates with ground-level ozone in Houston, Texas, J. Geophys. Res.: Atmos., 119, 6230-6245, https://doi.org/10.1002/2013jd020473, 2014.

Han, S., Bian, H., Tie, X., Xie, Y., Sun, M., and Liu, A.: Impact of nocturnal planetary boundary layer on urban air pollutants: Measurements from a 250-m tower over Tianjin, China, J. Hazard. Mater., 162, 264-269, https://doi.org/10.1016/j.jhazmat.2008.05.056, 2009.

Hua, Y., Wang, S., Wang, J., Jiang, J., Zhang, T., Song, Y., Kang, L., Zhou, W., Cai, R., Wu, D., Fan, S., Wang, T., Tang, X., Wei, Q., Sun, F., and Xiao, Z.: Investigating the impact of regional transport on PM2.5 formation using vertical observation during APEC 2014 Summit in Beijing, Atmos. Chem. Phys., 16, 15451-15460, https://doi.org/10.5194/acp-16-15451-2016, 2016.

Huang, X., Wang, Z., and Ding, A.: Impact of Aerosol-PBL Interaction on Haze Pollution: Multiyear Observational Evidences in North China, Geophys. Res. Lett., 45, 8596-8603, https://doi.org/10.1029/2018gl079239, 2018.

Jin-Xiang, L. I.: The Characteristics and Cause Analysis of Heavy-Air-Pollution in Autumn and Winter in Beijing, Environ. Monit. China, 2007.

Kotthaus, S., and Grimmond, C. S. B.: Atmospheric boundary-layer characteristics from ceilometer measurements. Part 1: A new method to track mixed layer height and classify clouds, Q. J. R. Meteorol. Soc., 144, 1525-1538, https://doi.org/10.1002/qj.3299, 2018.

Lee K., Li Z., Wong M., Xin J., Wang Y., Hao W., and Zhao F.: Aerosol single scattering albedo estimated across China from a combination of ground and satellite measurements, J. Geophys. Res.: Atmos., 112(D22), https://doi.org/10.1029/2007JD009077, 2007.

Levy, R. C., Remer, L. A., and Dubovik, O.: Global aerosol optical properties and application to Moderate Resolution Imaging Spectroradiometer aerosol retrieval

over land, J. Geophys. Res.: Atmos., 112, https://doi.org/10.1029/2006jd007815, 2007.

Li, G., Bei, N., Cao, J., Huang, R., Wu, J., Feng, T., Wang, Y., Liu, S., Zhang, Q., Tie, X., and Molina, L. T.: A possible pathway for rapid growth of sulfate during haze days in China, Atmos. Chem. Phys., 17, 3301-3316, https://doi.org/10.5194/acp-17-3301-2017, 2017.

Li, M., Wang, L., Liu, J., Gao, W., Song, T., Sun, Y., Li, L., Li, X., Wang, Y., Liu, L., Daellenbach, K. R., Paasonen, P. J., Kerminen, V.-M., Kulmala, M., and Wang, Y.: Exploring the regional pollution characteristics and meteorological formation mechanism of $PM_{2.5}$ in North China during 2013-2017, Environ. Int., 134, https://doi.org/10.1016/j.envint.2019.105283, 2020.

Li, Z., Lee, K.-H., Wang, Y., Xin, J., and Hao, W.-M.: First observation-based estimates of cloud-free aerosol radiative forcing across China, J. Geophys. Res.: Atmos., 115, https://doi.org/10.1029/2009jd013306, 2010.

Liu, Q., Jia, X., Quan, J., Li, J., Li, X., Wu, Y., Chen, D., Wang, Z., and Liu, Y.: New positive feedback mechanism between boundary layer meteorology and secondary aerosol formation during severe haze events, Sci. Rep., 8, https://doi.org/10.1038/s41598-018-24366-3, 2018.

Liu, T. T., Gong, S., Meng, Y., Qi, C. Z., and Hong, L. L.: Contributions of meteorology and emission to the 2015 winter severe haze pollution episodes in Northern China, Atmos. Chem. Phys., 17, 1-17, https://doi.org/10.5194/acp-2016-204, 2016.

Münkel, C., Eresmaa, N., Rasanen, J., and Karppinen, A.: Retrieval of mixing height and dust concentration with lidar ceilometer, Bound.-Layer Meteorol., 124, 117-128, https://doi.org/ 10.1007/s10546-006-9103-3, 2007.

Ma, Q., Wu, Y., Zhang, D., Wang, X., and Zhang, R.: Roles of regional transport and heterogeneous reactions in the $PM_{2.5}$ increase during winter haze episodes in Beijing, Sci. Total Environ., 599-600, 246-253, https://doi.org/10.1016/j.scitotenv.2017.04.193, 2017.

Miao, Y., Guo, J., Liu, S., Zhao, C., Li, X., Zhang, G., Wei, W., and Ma, Y.: Impacts of

synoptic condition and planetary boundary layer structure on the trans-boundary aerosol transport from Beijing-Tianjin-Hebei region to northeast China, Atmos. Environ., 181, 1-11, https://doi.org/10.1016/j.atmosenv.2018.03.005, 2018.

Munro, D. S.: Boundary Layer Climatology, 2005.

Niu, F., Li, Z., Li, C., Lee, K.-H., and Wang, M.: Increase of wintertime fog in China: Potential impacts of weakening of the Eastern Asian monsoon circulation and increasing aerosol loading, J. Geophys. Res.: Atmos., 115, https://doi.org/10.1029/2009jd013484, 2010.

Petaja, T., Jarvi, L., Kerminen, V. M., Ding, A. J., Sun, J. N., Nie, W., Kujansuu, J., Virkkula, A., Yang, X. Q., Fu, C. B., Zilitinkevich, S., and Kulmala, M.: Enhanced air pollution via aerosol-boundary layer feedback in China, Sci. Rep., 6, https://doi.org/10.1038/srep18998, 2016.

Pichugina, Y. L., Banta, R. M., Bonin, T., Brewer, W. A., Choukulkar, A., McCarty, B. J., Baidar, S., Draxl, C., Fernando, H. J. S., Kenyon, J., Krishnamurthy, R., Marquis, M., Olson, J., Sharp, J., and Stoelinga, M.: Spatial Variability of Winds and HRRR-NCEP Model Error Statistics at Three Doppler-Lidar Sites in the Wind-Energy Generation Region of the Columbia River Basin, J. Appl. Meteorol. Climatol., 58, 1633-1656, https://doi.org/10.1175/jamc-d-18-0244.1, 2019.

Quan, J., Gao, Y., Zhang, Q., Tie, X., Cao, J., Han, S., Meng, J., Chen, P., and Zhao, D.: Evolution of planetary boundary layer under different weather conditions, and its impact on aerosol concentrations, Particuology, 11, 34-40, https://doi.org/10.1016/j.partic.2012.04.005, 2013.

Robert, and Aron: Mixing height—an inconsistent indicator of potential air pollution concentrations, Atmos. Environ., 17, 2193-2197, https://doi.org/10.1016/0004-6981(83)90215-9, 1983.

Schaefer, K., Wang, Y., Muenkel, C., Emeis, S., Xin, J., Tang, G., Norra, S., Schleicher, N., Vogt, J., and Suppan, P.: Evaluation of continuous ceilometer-based mixing layer heights and correlations with $PM_{2.5}$ concentrations in Beijing, in: Remote Sensing of Clouds and the Atmosphere Xiv, edited by: Picard, R. H., Schafer, K.,

Comeron, A., Kassianov, E., and Mertens, C. J., Proceedings of SPIE, 2009.

Silvanus, P. T. F. R. S., and Gardner, M.: A Little More about Curvature of Curves, Calculus Made Easy, 249-262, https://doi.org/10.1007/978-1-349-15058-8_25, 1998.

Stone, R. S., Anderson, G. P., Shettle, E. P., Andrews, E., Loukachine, K., Dutton, E. G., Schaaf, C., and Roman, M. O., III: Radiative impact of boreal smoke in the Arctic: Observed and modeled, J. Geophys. Res.: Atmos., 113, https://doi.org/10.1029/2007jd009657, 2008.

Stull, R. B.: An Introduction to Boundary Layer Meteorology, 1988.

Su, T., Li, Z., and Kahn, R.: Relationships between the planetary boundary layer height and surface pollutants derived from lidar observations over China: regional pattern and influencing factors, Atmos. Chem. Phys., 18, 15921-15935, https://doi.org/10.5194/acp-18-15921-2018, 2018.

Tang, G., Zhu, X., Hu, B., Xin, J., Wang, L., Münkel, C., Mao, G., and Wang, Y.: Impact of emission controls on air quality in Beijing during APEC 2014: lidar ceilometer observations, Atmos. Chem. Phys., 15, 12667–12680, https://doi.org/10.5194/acp-15-12667-2015, 2015.

Tang, G., Zhang, J., Zhu, X., Song, T., Muenkel, C., Hu, B., Schaefer, K., Liu, Z., Zhang, J., Wang, L., Xin, J., Suppan, P., and Wang, Y.: Mixing layer height and its implications for air pollution over Beijing, China, Atmos. Chem. Phys., 16, 2459-2475, https://doi.org/10.5194/acp-16-2459-2016, 2016.

Tie, X., Huang, R.-J., Cao, J., Zhang, Q., Cheng, Y., Su, H., Chang, D., Poeschl, U., Hoffmann, T., Dusek, U., Li, G., Worsnop, D. R., and O'Dowd, C. D.: Severe Pollution in China Amplified by Atmospheric Moisture, Sci. Rep., 7, https://doi.org/10.1038/s41598-017-15909-1, 2017.

Wang, J. Z., Gong, S. L., Zhang, X. Y., Yang, Y. Q., Hou, Q., Zhou, C. H., and Wang, Y. Q.: A Parameterized Method for Air-Quality Diagnosis and Its Applications, Adv. Meteorol., https://doi.org/10.1155/2012/238589, 2012.

Wang, X., Wei, W., Cheng, S., Li, J., Zhang, H., and Lv, Z.: Characteristics and

classification of PM 2.5 pollution episodes in Beijing from 2013 to 2015, Sci. Total Environ., 612, 170-179, https://doi.org/10.1016/j.scitotenv.2017.08.206, 2018.

Wang, Y., Yao, L., Wang, L., Liu, Z., Ji, D., Tang, G., Zhang, J., Sun, Y., Hu, B., and Xin, J.: Mechanism for the formation of the January 2013 heavy haze pollution episode over central and eastern China, Sci. China-Earth Sci., 57, 14-25, https://doi.org/10.1007/s11430-013-4773-4, 2014.

Wilcox, E. M., Thomas, R. M., Praveen, P. S., Pistone, K., Bender, F. A. M., and Ramanathan, V.: Black carbon solar absorption suppresses turbulence in the atmospheric boundary layer, Proc. Natl. Acad. Sci. U. S. A., 113, 11794-11799, https://doi.org/10.1073/pnas.1525746113, 2016.

Xin, J., Gong, C., Wang, S., and Wang, Y.: Aerosol direct radiative forcing in desert and semi-desert regions of northwestern China, Atmos. Res., 171, 56-65, https://doi.org/10.1016/j.atmosres.2015.12.004, 2016.

Xu, T., Song, Y., Liu, M., Cai, X., Zhang, H., Guo, J., and Zhu, T.: Temperature inversions in severe polluted days derived from radiosonde data in North China from 2011 to 2016, Sci. Total Environ., 647, 1011-1020, https://doi.org/10.1016/j.scitotenv.2018.08.088, 2019.

Yu, H., Liu, S., and Dickinson, R.: Radiative effects of aerosols on the evolution of the atmospheric boundary layer, J. Geophys. Res., 107(D12), 1, 4142–14, https://doi.org/10.1029/2001JD000754, 2002.

Yang, Y., Liao, H., and Lou, S.: Increase in winter haze over eastern China in recent decades: Roles of variations in meteorological parameters and anthropogenic emissions, J. Geophys. Res.: Atmos., 121, 13050-13065, https://doi.org/10.1002/2016jd025136, 2016.

Zhang, Q., Ma, Q., Zhao, B., Liu, X., Wang, Y., Jia, B., and Zhang, X.: Winter haze over North China Plain from 2009 to 2016: Influence of emission and meteorology, Environ. Pollut., 242, 1308-1318, https://doi.org/10.1016/j.envpol.2018.08.019, 2018.

Zhang, R., Khalizov, A. F., Pagels, J., Zhang, D., Xue, H., and McMurry, P. H.:

Variability in morphology, hygroscopicity, and optical properties of soot aerosols during atmospheric processing, Proc. Natl. Acad. Sci. U. S. A., 105, 10291-10296, https://doi.org/10.1073/pnas.0804860105, 2008.

Zhang, Z., Zhang, X., Zhang, Y., Wang, Y., Zhou, H., Shen, X., Che, H., Sun, J., and Zhang, L.: Characteristics of chemical composition and role of meteorological factors during heavy aerosol pollution episodes in northern Beijing area in autumn and winter of 2015, Tellus B, 69, https://doi.org/10.1080/16000889.2017.1347484, 2017.

Zhao, D., Xin, J., Gong, C., Quan, J., Liu, G., Zhao, W., Wang, Y., Liu, Z., and Song, T.: The formation mechanism of air pollution episodes in Beijing city: Insights into the measured feedback between aerosol radiative forcing and the atmospheric boundary layer stability, Sci. Total Environ., 692, 371-381, https://doi.org/10.1016/j.scitotenv.2019.07.255, 2019.

Zheng, C., Zhao, C., Zhu, Y., Wang, Y., Shi, X., Wu, X., Chen, T., Wu, F., and Qiu, Y.: Analysis of influential factors for the relationship between $PM_{2.5}$ and AOD in Beijing, Atmos. Chem. Phys., 17, 13473-13489, https://doi.org/10.5194/acp-17-13473-2017, 2017.

Zheng, G. J., Duan, F. K., Su, H., Ma, Y. L., Cheng, Y., Zheng, B., Zhang, Q., Huang, T., Kimoto, T., Chang, D., Poeschl, U., Cheng, Y. F., and He, K. B.: Exploring the severe winter haze in Beijing: the impact of synoptic weather, regional transport and heterogeneous reactions, Atmos. Chem. Phys., 15, 2969-2983, https://doi.org/10.5194/acp-15-2969-2015, 2015.

Zhong, J., Zhang, X., Wang, Y., Sun, J., Zhang, Y., Wang, J., Tan, K., Shen, X., Che, H., Zhang, L., Zhang, Z., Qi, X., Zhao, H., Ren, S., and Li, Y.: Relative Contributions of Boundary-Layer Meteorological Factors to the Explosive Growth of $PM_{2.5}$ during the Red-Alert Heavy Pollution Episodes in Beijing in December 2016, J. Meteorol. Res., 31, 809-819, https://doi.org/10.1007/s13351-017-7088-0, 2017.

Zhong, J., Zhang, X., Wang, Y., Liu, C., and Dong, Y.: Heavy aerosol pollution episodes in winter Beijing enhanced by radiative cooling effects of aerosols, Atmos. Res.,

209, 59-64, https://doi.org/10.1016/j.atmosres.2018.03.011, 2018a.

Zhong, J., Zhang, X., Dong, Y., Wang, Y., Liu, C., Wang, J., Zhang, Y., and Che, H.: Feedback effects of boundary-layer meteorological factors on cumulative explosive growth of PM2.5 during winter heavy pollution episodes in Beijing from 2013 to 2016, Atmos. Chem. Phys., 18, 247–258, https://doi.org/10.5194/acp-18-247-2018, 2018b.

Zhong, J., Zhang, X., Wang, Y., Wang, J., Shen, X., Zhang, H., Wang, T., Xie, Z., Liu, C., Zhang, H., Zhao, T., Sun, J., Fan, S., Gao, Z., Li, Y., and Wang, L.: The two-way feedback mechanism between unfavorable meteorological conditions and cumulative aerosol pollution in various haze regions of China, Atmos. Chem. Phys., 19, 3287–3306, https://doi.org/10.5194/acp-19-3287-2019, 2019.

Zhu, X., Tang, G., Lv, F., Hu, B., Cheng, M., Muenkel, C., Schafer, K., Xin, J., An, X., Wang, G., Li, X., and Wang, Y.: The spatial representativeness of mixing layer height observations in the North China Plain, Atmos. Res., 209, 204-211, https://doi.org/10.1016/j.atmosres.2018.03.019, 2018.